

Unsupervised Learning-Based Multiscale Model of Thermochemistry in 1,3,5-Trinitro-1,3,5-triazinane (RDX)

Michael N. Sakano, Ahmed Hamed, Edward M. Kober, Nicolo Grilli, Brenden W. Hamilton, Md Mahbubul Islam, Marisol Koslowski, and Alejandro Strachan*



Cite This: <https://dx.doi.org/10.1021/acs.jpca.0c07320>



Read Online

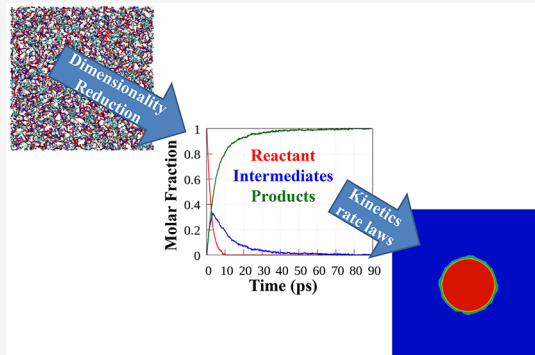
ACCESS |

Metrics & More

Article Recommendations

Supporting Information

ABSTRACT: The response of high-energy-density materials to thermal or mechanical insults involves coupled thermal, mechanical, and chemical processes with disparate temporal and spatial scales that no single model can capture. Therefore, we developed a multiscale model for 1,3,5-trinitro-1,3,5-triazinane, RDX, where a continuum description is informed by reactive and nonreactive molecular dynamics (MD) simulations to describe chemical reactions and thermal transport. Reactive MD simulations under homogeneous isothermal and adiabatic conditions are used to develop a reduced-order chemical kinetics model. Coarse graining is done using unsupervised learning via non-negative matrix factorization. Importantly, the components resulting from the analysis can be interpreted as reactants, intermediates, and products, which allows us to write kinetics equations for their evolution. The kinetics parameters are obtained from isothermal MD simulations over a wide temperature range, 1200–3000 K, and the heat evolved is calibrated from adiabatic simulations. We validate the continuum model against MD simulations by comparing the evolution of a cylindrical hotspot 10 nm in diameter. We find excellent agreement in the time evolution of the hotspot temperature fields both in cases where quenching is observed and at higher temperatures for which the hotspot transitions into a deflagration wave. The validated continuum model is then used to assess the criticality of hotspots involving scales beyond the reach of atomistic simulations that are relevant to detonation initiation.



1. INTRODUCTION

Shock-induced detonation of microstructurally complex high-energy-density (HE) materials and other initiation processes that involve mechanical stimuli involve the localization of energy into hotspots that accelerate the initiation of exothermic chemical reactions and their self-sustaining propagation. These hotspots result from the interaction of the propagating wave with microstructural features and defects; this is primarily through pore collapse, though other processes such as interfacial friction, localized plastic deformation, and shearing along cracks are also possible.^{1–3} The latter mechanisms are also quite significant for accidental/mechanical initiation processes and the initiation of more sensitive primary explosives. Thus, the predictive models of detonation initiation (and failure) require a description of mechanical, thermal, and chemical processes under extreme conditions of temperature, pressure, and loading rates and should capture the effect of microstructures and defects. The underlying processes span disparate temporal and spatial scales, from bond breaking and formation at angstroms and femtoseconds, to hotspots and microstructures ranging from tens of nanometers to tens of microns and up, to run to detonation distances of up to several centimeters.^{4–6} Although reactive molecular dynamics (MD) simulations can provide an explicit description of all the individual processes, the scales

involved in detonation initiation, steady propagation, and failure are beyond their reach for the foreseeable future. Therefore, a predictive understanding of the initiation of HE materials, capable of modeling shock-to-detonation or other initiation events with chemistry and microstructures as only inputs, requires a multiscale approach, where information from atomistic simulations can be used to inform and parameterize a continuum model. Despite significant progress over decades, we lack such multiscale models capable of capturing thermomechanical properties and chemistry under extreme conditions and in microstructurally complex systems. With this as our ultimate goal, we present a multiscale model capable of describing the evolution of hotspots in 1,3,5-trinitro-1,3,5-triazinane, RDX, parameterized from extensive MD simulations using unsupervised learning for coarse graining.

Current continuum-level models of detonation initiation and failure^{7–15} are generally based on the statistical description of

Received: August 10, 2020

Revised: October 1, 2020

hotspots and are parameterized against experiments. Mesoscale models are making progress in quantifying how the interaction of shockwaves with defects and microstructures results in the formation of hotspots^{16–20} but cannot accurately describe the transition to detonation.^{4,5,21,22} At smaller scales, reactive MD simulations have captured the shock-to-deflagration transition following the dynamical formation of hotspots from void collapse.^{23,24} Predictive models would require informing continuum thermo-chemo-mechanical models from first principles and mapping microstructures and defects to hotspots from atomistic and mesoscale simulations. The development and validation of such models is hindered by the lack of experimental tools with the resolution required to capture the formation of hotspots and their role in detonation initiation. There has been significant recent progress in the measurement of temperature associated with hotspots via emission spectroscopy,²⁵ but these measurements lack spatial resolution or the ability to separate the initial temperature increase during the formation of the hotspot and that associated with sustaining exothermic chemical reactions.²⁶ Thus, these measurements cannot be directly used to assess which hotspots become critical and sustain a developing detonation.²⁷ In summary, there remain large gaps in our knowledge of quantitatively predicting detonation development. In this paper, we use a combination of reactive and nonreactive simulations to inform a continuum model concerning the hotspot characteristics for RDX.

Atomistic simulations using either ab initio methods such as density functional theory (DFT), tight binding potentials, or reactive force fields have contributed greatly to our understanding of the chemistry, thermomechanics, and the coupling thereof. Early work focused on gas phase reactions^{28,29} using DFT and molecular dynamics of small condensed matter samples subjected to thermal^{30,31} or shock loading.³² Advances in hardware and algorithms have enabled, in recent years, condensed matter simulations at the DFT level³³ and using tight binding,^{34,35} though the small sample sizes present problems for proper extrapolation. Large-scale reactive and nonreactive simulations enable the direct coupling of mechanical deformation and heat generation processes by means of shock-induced defects,³⁶ hotspots^{26,37} and the shock-to-deflagration transition^{23,24} following the collapse of porosity. Reactive MD simulations provide insights into the molecular-level processes of decomposition,^{38,39} and in combination with ultra-fast spectroscopy experiments on laser-driven shocks^{40–42} are enabling, for the first time, a direct (if not perfect) comparison of chemical reactions under the appropriate extreme conditions.

Despite this progress, atomistic simulations lack the ability to capture microstructural effects with feature sizes above a micron, limiting their ability to model realistic microstructures of HE formulations; thus, significant efforts have been made in the meso and macroscopic modeling of initiation. A fascinating evaluation of hotspot reaction kinetics for HMX and TATB was developed by Tarver et al. established from time-to-explosion measurements of different sized samples.²⁷ They used a three-step, four-component scheme to describe the reaction kinetics for both materials, based on Arrhenius kinetics. Each reaction has an associated specific heat of reaction, although information concerning pressure is absent. Their combined kinetics and heat diffusion model were calibrated from time-to-thermal explosion data within the temperature regime of 450–600 K and extrapolated to higher temperatures appropriate for the rapid hotspot development (1000–2000 K). The authors used this model to determine the critical or threshold hotspot temper-

ature required to transition into a deflagration wave as a function of hotspot size and geometry. An interesting aspect was that the initial reactions for both HMX and TATB were found to be endothermic, which would suppress further reactions under moderate conditions. Henson and Smilowitz have further developed a more elaborate model for the decomposition and reaction of HMX that accounts for the β -HMX to δ -HMX transition, solid to gas decomposition, and gas phase ignition.⁴³ This model includes competing pathways that could become dominant under different pressure regimes, though this was not quantified. Maillet et al. developed a reactive dissipative particle dynamics model for shocked liquid nitromethane.⁴⁴ They coupled the hydrodynamical features of dissipative particle dynamics with chemical reactions by coarse-graining the molecules to reduce chemical complexity. Nitromethane chemistry was represented as two first-order reactions, the first step being reversible and endothermic, while the second step irreversible and exothermic. The kinetics prefactor used in the simulations was artificially accelerated so that the timescales associated with chemistry matched the total simulation time achievable. The authors observed a shock-induced reactive wave progressively catching up with the shock wave, eventually resulting in a detonation.

The examples above used experiments to parameterize reduced-order chemistry models. Being able to obtain such models from first principles-based atomistic simulations is an attractive alternative since it would enable the exploration of new materials, not yet synthesized. One such example is the work of Stewart and co-workers⁴⁵ who used reactive MD simulations for the ignition and growth for a three-dimensional hotspot to develop a chemical kinetics model. The authors coarse-grained the MD results by establishing four groups of molecules approximately corresponding to RDX, polyradicals, intermediates, and products. They used a formulation based on the Gibbs free energy and parameterized a kinetics model for the evolution of the first three components with respect to pressure and temperature. Enthalpic contributions to the Gibbs free energy were captured using a nonideal gas law. The model matched mass fractions and average temperature and pressure from the MD decomposition simulations under adiabatic conditions (NVE ensemble) starting from the induction phase. However, no further comparisons or independent validation tests were conducted outside of the conditions used for parameterization.

In this paper, we present a multiscale model for RDX that combines MD simulations of thermal transport and chemical decomposition with a continuum model using finite elements that captures all of these processes. Importantly, we use unsupervised learning to perform dimensionality reduction of the MD trajectories to derive a reduced-order chemical reaction model that optimally describes decomposition and reactions predicted by the atomistic simulations. A chemical kinetics model is then parameterized from isothermal and adiabatic MD simulations using these components; the model accurately captures the homogeneous decomposition of RDX in a wide temperature range. The continuum model also incorporates thermal transport parameterized from the MD simulations. The continuum model is used to assess the critical temperature required for hotspots to transition into deflagration waves for sizes ranging from 10 nm to 1 μm in diameter. For nanoscale hotspots, we compare the predictions of the model with explicit MD simulations (not used in the parameterization) and find good agreement; this represents an important validation of our

approach. In addition to the chemistry and thermal transport demonstrated in this paper, a continuum level model capable of describing shock-induced chemistry should incorporate equations of state to describe the shock state, plasticity, and fracture.^{16,46,47} These physics have been incorporated in our software, see refs.,^{20,48,49} but will not be used in this paper.

The remainder of the paper is organized as follows. **Section 2** describes the MD simulations used to develop the model, whereas **Section 3** discusses the chemical kinetics model and extracting both rate parameters and heat of reaction coefficients. **Section 4** covers the continuum model and mesoscale hotspot systems, and in **Section 5**, we validate the nanoscale hotspots from MD. We conduct a sensitivity analysis of the parameters feed into our continuum model at larger scales in **Section 6** and provide concluding remarks in **Section 7**.

2. ATOMISTIC SIMULATIONS AND MODEL DETAILS

The multiscale model builds on MD simulations of thermal properties and chemical decomposition. **Subsection 2.1** describes the simulation details and **subsection 2.2** covers the thermal properties for thermal conductivity and specific heat.

2.1. Homogeneous Decomposition and Reaction Simulations. The reduced-order chemical kinetics model is derived from isothermal and adiabatic reactive MD simulations for a wide range of temperatures.

2.1.1. ReaxFF Force Field. To describe the atomic interactions and account for bond breaking and formation events, we use the reactive force field ReaxFF.⁵⁰ This method uses partial bond orders to characterize covalent interactions as well as polarizable charges computed at every time step to describe electrostatics. In this study, the parameterization by Wood et al.⁵¹ denoted as ReaxFF-2014 was selected to describe the chemical decomposition of RDX. More recently, this force field was used to study the decomposition of nitromethane,⁴² where timescales for predicting various shock strengths required to induce chemical reactions were in good agreement with mid-IR spectroscopy studies on laser-shocked samples. All MD simulations were performed using LAMMPS (version 16Mar2018), a parallel MD software package from Sandia National Laboratories.⁵² We note that this force field is not without limitations as has been documented in previous works^{18,42} but our main goal is to develop and validate an approach for multiscale modeling and not to provide the most accurate model for RDX.

2.1.2. Sample Preparation. The procedures for creating supercells of the crystalline RDX sample at experimental density can be found in our previous publication.³⁸ Briefly, we obtained a unit cell of RDX⁵³ from the Cambridge Crystallographic Data Centre, replicated the unit cell $3 \times 3 \times 3$ times, and relaxed the resulting supercell via energy minimization. This simulation cell, containing 216 molecules or 4536 atoms, was used for homogeneous decomposition simulations. Previous hotspot simulations detailed in the same study were used for the validation of the continuum model. These larger systems were created by replicating the RDX unit cell $33 \times 36 \times 3$ times (28,512 molecules or 598,752 atoms), energy minimizing the supercell, and heating a cylindrical core with a diameter of 10 nm in size to a specified target temperature under NVT conditions before allowing the entire system to evolve using the NVE ensemble.

2.1.3. Homogeneous Decomposition Simulations. To simulate the isothermal decomposition of our crystalline structures relaxed at $T = 300$ K, the samples had their velocities

set to match the desired temperatures (1200, 1300, 1400, 1500, 1600, 1700, 1800, 2000, 2250, 2500, 2750, and 3000 K), and following this instantaneous heating, a Nosé–Hoover thermostat was applied to maintain isothermal conditions. The simulations were continued until chemical reactions were complete and the potential energy reached steady-state conditions. The total simulation time ranged between 100 ps and 10 ns. In another set of simulations, we enforced adiabatic conditions after samples had their initial velocities seeded to double their target temperatures ($T_0 = 2400, 2600, 2800$ K, etc.). Due to energy equipartition, the system temperature settled to (approximately) the desired value within 0.1 ps. In the hotter systems, the integration timestep was decreased to conserve energy as follows: 0.1 fs for $T_0 < 1800$ K, 0.05 fs for $1800 \text{ K} \leq T_0 < 2400$ K, and 0.025 fs for $2400 \text{ K} \leq T_0$.

2.2. Thermal Transport and Thermodynamic Properties.

2.2.1. Thermal Conductivity. Thermal conductivity was computed for RDX along the [100] direction using non-equilibrium MD simulations as detailed in our previous publication.³⁸ These simulations were performed using the nonreactive force field by Smith and Bharadwaj⁵⁴ due to reduced computational costs when compared to ReaxFF. We used a reverse nonequilibrium molecular dynamics method by Müller-Plathe to swap atomic velocities and impose a heat flux.⁵⁵ Upon reaching a steady-state temperature gradient, Fourier's Law was applied to extract thermal conductivity. The values were calculated for multiple samples of various transport lengths since it has been reported that thermal conductivity in nanoscale samples is strongly size-dependent due to ballistic effects.⁵⁶ Values used are present in the Supporting Information of ref 38. The thermal conductivity of crystalline RDX as a function of system size along the [100] transport direction is given by the following expression: $\frac{1}{\kappa} = \left(\frac{32.7}{L \text{ [nm]}} + 1.68 \right) \left[\frac{m - K}{W} \right]$. Compared with the work by Izvekov et al.,⁵⁷ although our values are roughly $0.1 \frac{W}{m - K}$ larger for the same transport length, we still show good agreement in nanoscale heat transport. We note that we ignore the role of chemical reactions on thermal conductivity.

2.2.2. Specific Heat. The continuum level model requires the specific heat of the material at any stage of decomposition, that is, as a function of the population of each of the components used to describe the progress of the chemical reactions. MD simulations use classical mechanics and result in classical statistical mechanics; the associated specific heat can be accurately approximated by the classical harmonic value of $\frac{1}{2}k_B T$ per degree of freedom. This classical value is known to significantly overestimate the actual value for molecular materials, governed by quantum statistical mechanics. Thus, to improve the accuracy of our continuum model, we computed the specific heat for each of the components of the reduced chemical kinetics model based on quantum statistical mechanics. The contribution to the total specific heat of the species belonging to each component was calculated from the rotovibrational density of states of the corresponding atoms from isothermal simulations using the following equation:⁵⁸

$$C_v = k_B \int_0^{\infty} d\omega \cdot S(\omega) \cdot \frac{\hbar^2 \omega^2 e^{\hbar\omega/k_B T}}{(k_B T)^2 (1 - e^{-\hbar\omega/k_B T})^2} \quad (1)$$

where k_B is the Boltzmann constant, \hbar is the reduced Planck constant, and $S(\omega)$ is the phonon density of states. $S(\omega)$ is obtained from the Fourier transform of the velocity

autocorrelation function.⁵⁹ The resulting data for each component was fitted using the functional form:

$$C_{v,\text{component } i}(T) = \frac{1}{(1 + T^a)^b} \quad (2)$$

Validation of our chemical component heat capacities will be addressed in subsection 3.5.

3. REDUCED CHEMICAL KINETICS MODEL

This section describes the use of unsupervised learning to develop a reduced chemical kinetics model for RDX based on MD simulations and its parameterization. Subsection 3.1 introduces the dimensionality reduction technique used to coarse grain the reactive chemistry, subsection 3.2 provides the thermochemical model, subsections 3.3 and 3.4 cover extracting the parameters and verifying the values, and subsection 3.5 details the results for our chemical component heat capacities.

3.1. Dimensionality Reduction via Unsupervised Machine Learning. Our goal is to develop a reduced-order chemical kinetics model based on reactive MD simulations for the decomposition and reaction of RDX. A key challenge is dimensionality reduction, i.e., how to condense down the detailed information in the MD simulation into a few key descriptors (components) of the state of the system whose time evolution can be described with physics-based kinetics laws. Our approach involves three steps: (i) selecting appropriate descriptors for the MD simulation results, (ii) using data science methods to perform dimensionality reduction where the full information will be encoded into a few components that capture the main trends in the data, and (iii) obtaining kinetics equations to describe the evolution of the components as a function of temperature from our isothermal simulations.

3.1.1. Descriptors of the Reactive MD Simulations. One could, in principle, use the raw atomic positions of all atoms as the description, but it is well established that using descriptors with physical meaning is very valuable in machine learning exercises.^{60–62} A better choice would be to use the population of the various molecules that form during the simulation. However, the dimensionality of the problem would be quite high due to the large number of molecules, radicals, and clusters that form when HE materials decompose at high pressures. Further, extracting knowledge from these population distributions is problematic at best. Instead, we use an approach based on coordination geometry analysis (CGA), which focuses on the bonding environments of each atom. This is related to the classic group additivity method developed by Benson to estimate heats of formations and other physical properties.^{63,64} However, because of the high temperatures of the reacting systems and the presence of numerous radicals, it is difficult to define accurate bond orders and precisely define the chemical groups. Instead, we simply rely on totaling the number and types of atoms that are bound to a given central atom, which defines its basic coordination geometry. In this framework, the initial structure of RDX would be described as 6 O[N], 3 N[NOO], 3 N[CCN], 3 C[HHNN], and 6 H[C]. The major products such as N₂, H₂O, and CO would be described as 2 N[N], O[HH] + 2 H[O], and C[O] + O[C], respectively. Given conventional organic chemistry, each atom will have no more than four bonds (and H would be unlikely to have more than one). For HCNO systems, this defines a total of 280 different coordination geometries. Our reactive MD simulations can thereby be reduced to a matrix containing the population of all 280 bonding

environments (columns) as a function of time (rows). While the population of bonding environments is described with integer numbers greater or equal to zero, the large simulation cells result in smooth evolution amenable to dimensionality reduction techniques. The ReaxFF method automatically tracks the bond order (BO) between atoms, and we simply filter those for BO ≥ 0.5 as the bond cutoff definition. Given the similarity to the group additivity methods, this method should track the heat of reaction reasonably well. Within this framework, we can also track the net sense of the reaction state (e.g., when C is first being oxidized or when N₂ is produced). From further correlations of bonding changes and establishing bond networks, one could extract more detailed reaction descriptions, but this is beyond the level of information we need for this study. One could use molecular populations instead of the bonding environments, but the extraordinarily large number of possible molecules (including clusters) makes the use of bonding environment attractive.

3.1.2. Dimensionality Reduction via Non-negative Matrix Factorization. The next step is to reduce the dimensionality of the problem from 280 to a more manageable number that can be used in continuum simulations. We achieve this by applying a dimensionality reduction algorithm using unsupervised learning to our bonding environment matrix X (which contains all 280 different bonding environments as a function of time). Techniques for dimensionality reduction aim to project the information to a lower dimensional space, either for simplification or for disclosing only the dominating pieces of data. A popular technique is principal component analysis (PCA)^{65,66} which uses singular value decomposition to factorize the input matrix into a product of two submatrices. One of the matrices contains the eigenvalue solutions, of which the contents include any rational number. However, in our context, it is preferable for interpretability that the encoded matrix contains non-negative values (the population of averaged components should not be negative). Therefore, we chose non-negative matrix factorization (NMF)^{67,68} as our dimensionality reduction method. NMF has been shown to help with interpretability of image recognition processes^{69–71} and we hypothesized that the same could occur in our application. The codes to perform and compare both PCA and NMF analysis on an example data set are available for online interactive computing in nanoHUB.⁷²

As stated above, matrix X contains all 280 different bonding environments as a function of time. This matrix of dimension ($t \times 280$), t being the number of timeframes in the simulation, can be decomposed into a product of two submatrices, W ($t \times d$) and H ($d \times 280$). Matrix W describes the time evolution of each of the $d (>1)$ components, and each of the d rows of H describes the components in terms of bond populations. For example, one would expect the atomic environment describing N₂ or N[N], a final product, to belong to a component that starts at zero and grows over time as this gas forms. It is important to stress that the composition of each component does not evolve during the decomposition and subsequent reactions and is temperature-independent; what evolves with time is the population of each of these components. One metric to determine the goodness or quality of the factorization is to calculate the residuals in the time evolution between the input matrix X and the predicted/decoded matrix $\hat{X} = W \times H$ for each bonding environment. This tests the decoder by determining how well the NMF solution preserves the original raw data. In context, it can give an indication of how many components are required to accurately reproduce the data.

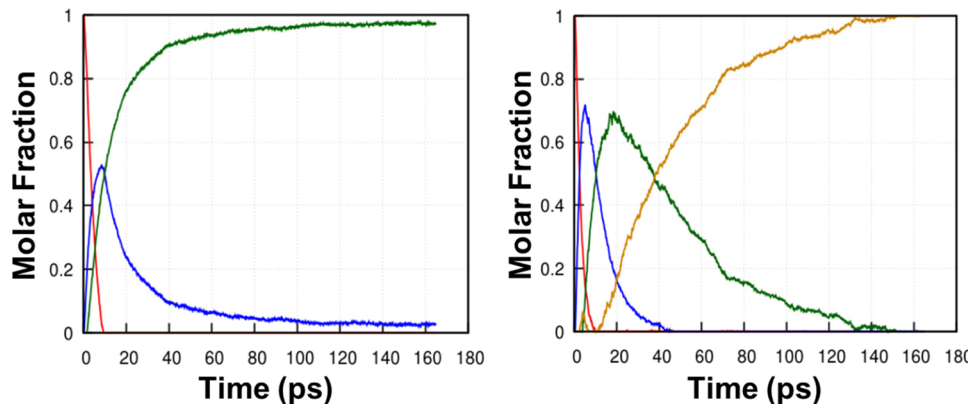


Figure 1. Three- and four-component fits for isothermal decomposition at 2500 K. Choosing three components allows for a naïve, but simplistic categorization of the chemistry into reactants, intermediates, and final products.

3.1.3. Three-Component Approach. Using NMF, we can decompose our bond environment matrix to obtain the time evolution for an arbitrary number of components. Since we are interested in extracting chemical kinetics parameters, we apply the NMF method to our isothermal simulations. We analyze the results of all temperatures to obtain a single set of components to describe the range of conditions studied. The time evolution of each component obtained from a three- and four-component factorization, after postprocessing, is shown in Figure 1 for a simulation at $T = 2500$ K. Importantly, components resulting from the NMF show the expected evolution for reactants, intermediates, and final gases in the context of decomposition chemistry, which is critical to designating kinetics laws. In the limit of a perfect fit, the sum of the contributions from the different components should add exactly to 1, but for a finite number of components, this sum will be $1 \pm \delta$, where δ represents an error metric that is typically only a few percent. Our fitting procedure requires the summation to be exactly 1; hence, the data at each time step was normalized to achieve this. As such, all values lie between 0 and 1, inclusive.

To obtain the right balance between the computational simplicity of the coarse-grained models and accuracy, we conducted the NMF analysis for a number of components from two to five for each isothermal temperature system and computed the root-mean-square error (RMSE). This is computed between the actual population of the bonding environments in the MD simulations (\mathbf{X}) and the result from the product of the encoded matrix and the population of each component $\mathbf{W} \times \mathbf{H}$, averaged over all times and temperatures. Additional details of this calculation are included in Section S3 of the Supporting Information. As expected, increasing the number of components results in lower RMSE, see Figure 2. Interestingly, we find an important reduction in the RMSE from two to three components and less, hence, moving to four or five. Thus, the remainder of the paper will use three components. This choice will be further justified *a posteriori* when we show the resulting kinetics model to be in good agreement with the all-atom simulations.

Beyond confirming the expected overall time evolution of the three components, we analyzed the bond environments associated with each of them. The dominant environments in the first component are O[N], N[NOO], N[NCC], C[NNHH], and H[C], all of which are the structural features present in RDX. The second component is composed of N[O], N[OO], O[HN], H[O], O[N], and O[NN], all of which define common intermediates such as NO, NO₂, HONO, OH, and

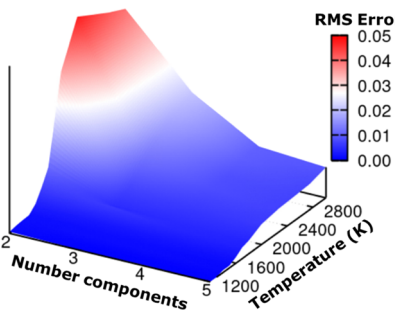


Figure 2. Root-mean square error fitting all 280 bonding environments for two to five components.

N₂O. The third component is dominated by C[OO], O[HH], and N[N], which reflect CO₂, H₂O, and N₂ species, respectively. An example case of formulating a three-component fit from a 3000 K simulation bond table using this NMF algorithm can be found in the [Supporting Information](#) and the nanoHUB tool cited above.

3.2. Reduced-Order Chemical Kinetics. In this section, we propose and parameterize a set of kinetics equations to describe the time evolution of the three components identified for RDX as well as the associated heat evolved. We describe the evolution of the three components via a two-step model with sequential, irreversible, first-order reactions: $C_1 \rightarrow C_2 \rightarrow C_3$, where the components C_i represent the molar fractions of the three components (reactant, intermediates, and products).

The rate equations are as follows:

$$\dot{C}_1 = -C_1 Z_a \exp\left(-\frac{E_a}{RT}\right) \quad (3a)$$

$$\dot{C}_2 = C_1 Z_a \exp\left(-\frac{E_a}{RT}\right) - C_2 Z_b \exp\left(-\frac{E_b}{RT}\right) \quad (3b)$$

$$\dot{C}_3 = C_2 Z_b \exp\left(-\frac{E_b}{RT}\right), \quad (3c)$$

where R is the gas constant, Z_a and Z_b are the frequency prefactors, and E_a and E_b are the activation energies of the two reaction steps. The heat evolved during the reactions is coupled to the temperature evolution as:

$$\rho C_v \dot{T} = -Q_1 \dot{C}_1 + Q_2 \dot{C}_3, \quad (4)$$

where ρ is the system density, C_v is the classical specific heat, and Q_1 and Q_2 are the heat of reaction coefficients to be parameterized from the MD simulations. Based on the analysis of our simulations, we find the need for Q_i to be temperature dependent and have the form:

$$Q_i(T) = \begin{cases} a_1 & \text{if } T \leq T_{\text{ref}} \\ a_1 + b_1(T - T_{\text{ref}}) & \text{if } T \geq T_{\text{ref}} \end{cases} \quad (5)$$

where a_1 and b_1 are fitted coefficients to be extracted and T_{ref} is the critical temperature where the heat of reaction transitions from a constant at lower temperatures to linear dependence at higher temperatures.

3.3. Calibration and Testing. The parameters of the kinetics model (prefactors and activation energies) were extracted from the time evolution of each component at the various temperatures. We define two Arrhenius equations as follows:

$$\beta(T) = Z_a \exp\left(-\frac{E_a}{RT}\right)$$

$$\gamma(T) = Z_b \exp\left(-\frac{E_b}{RT}\right)$$

and note that $T \cdot \ln[\beta(T)]$ and $T \cdot \ln[\gamma(T)]$ are linear functions of temperature. The Supporting Information describes additional details of the algorithm used. The interpolants for our kinetics parameters are shown as blue circles and squares in Figure 3, and the lines represent the fitted model. Table 1 shows the resulting kinetics parameters.

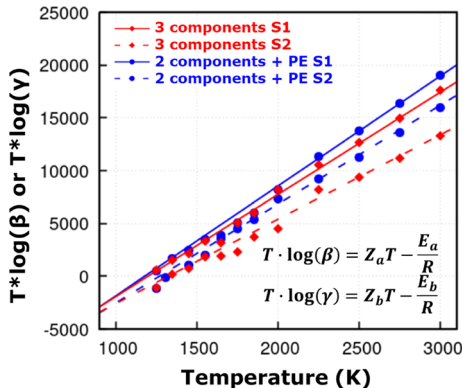


Figure 3. Linear fit for kinetics parameters describing the two-step decomposition model of RDX using the ReaxFF-2014 force field. The pre-factor correlates with the slope, and the activation energy correlates with the y -intercept.

To improve the description of heat evolved during reactions, we modified the three-component fit by replacing the third component (representing products) with the scaled and normalized potential energy (PE) profile. As will be discussed later, this change improves the description of the kinetics and heat evolved in the system. Other references in the literature have used the PE curve to represent the single-step decomposition for the whole system.^{31,73} To obtain the third component, the PE evolution in the simulation is shifted by its initial value such that it begins at 0. At each time step, the modified PE value is scaled by the total exothermicity or change in energy due to reaction, and has its sign changed so all values fall between 0 and 1. This process ensures that the scaled PE

Table 1. Kinetics Parameters Obtained from Two Different Models: Three Components (Model 1) and Two Components + Potential Energy (Model 2) with 95% Confidence Interval^a

model	step	$\ln(Z_i[\text{s}^{-1}])$	$E_i[\text{kcal/mol}]$
1	$C_1 \rightarrow C_2$	30.4 ± 0.5	23.0 ± 1.8
	$C_2 \rightarrow C_3$	28.7 ± 0.6	20.9 ± 2.0
2	$C_1 \rightarrow C'_2$	31.1 ± 0.4	24.4 ± 1.5
	$C'_2 \rightarrow \text{PE}$	30.1 ± 0.4	23.5 ± 1.6

^aIn Model 1, the concentration profiles are taken directly from the NMF method. In Model 2, the third component is replaced with a modified potential energy curve, and component 2 is recalculated to match the sum $C_1 + C_2 + \text{PE} = 1$. Model 2 provides a lower RMS error when considering all temperatures in our isothermal simulations; therefore, it will be used for the remainder of the paper.

curve retains the overall shape of the NMF third component but approaches the value of 1 at a slightly faster rate, which is important when considering the heat evolved. To obtain the change in energy, we fit an exponential decay function to the potential energy curve after ignoring the first 0.1 ps for each isothermal simulation. Red markers and lines in Figure 3 show the fits for this new model (two components + PE), and the parameters are included in Table 1.

As stated above, we observe that replacing the third component with the scaled PE improves the overall agreement between the model and the MD simulations. We attribute this to the fact that the potential energy evolves from the start of the simulation while the product component, C_3 , remains at zero for a short induction time, see Figure 1. In addition, the various chemical processes grouped together to define the formation of products in our reduced-chemistry model can have slightly different timescales and contributions to the exothermicity. This induction time increases with decreasing temperature and cannot be captured by our simple three-species two-reaction model. Therefore, by replacing the product curve with the modified PE profile, the overall fitting of the kinetics scheme is improved, see Figure 4. Also shown in the figure are the RMSE values for each isothermal simulation. Interestingly, the accuracy of the model degrades slightly at lower initial temperatures, which could be a consequence that a simple sequential, irreversible, first-order reaction model is not enough to match the induction behavior of the MD data. The calculation for each isotherm's RMS error is explained in the Supporting Information. We find that, despite its simplicity, the model captures the overall behavior for the reactants, intermediates, and final products. The calibrated three-component fit (no potential energy) for each temperature is included in the Supporting Information, Figure S1. We foresee that describing chemical processes with vastly different timescales that occur in certain HE materials, such as the slow process of carbon clustering, will likely require an additional component describing these products. Future work on TATB decomposition will investigate these issues.

The kinetics model developed from isothermal simulations was validated against adiabatic simulations. We applied the same NMF plus potential energy analysis to the adiabats and compared their time evolution to the predictions of the kinetics models. We used the MD bulk temperature to evolve the kinetics at each time step. A comparison between the model and simulation data is shown in the Supporting Information, Figure S2. While we underfit the lower-temperature transients,

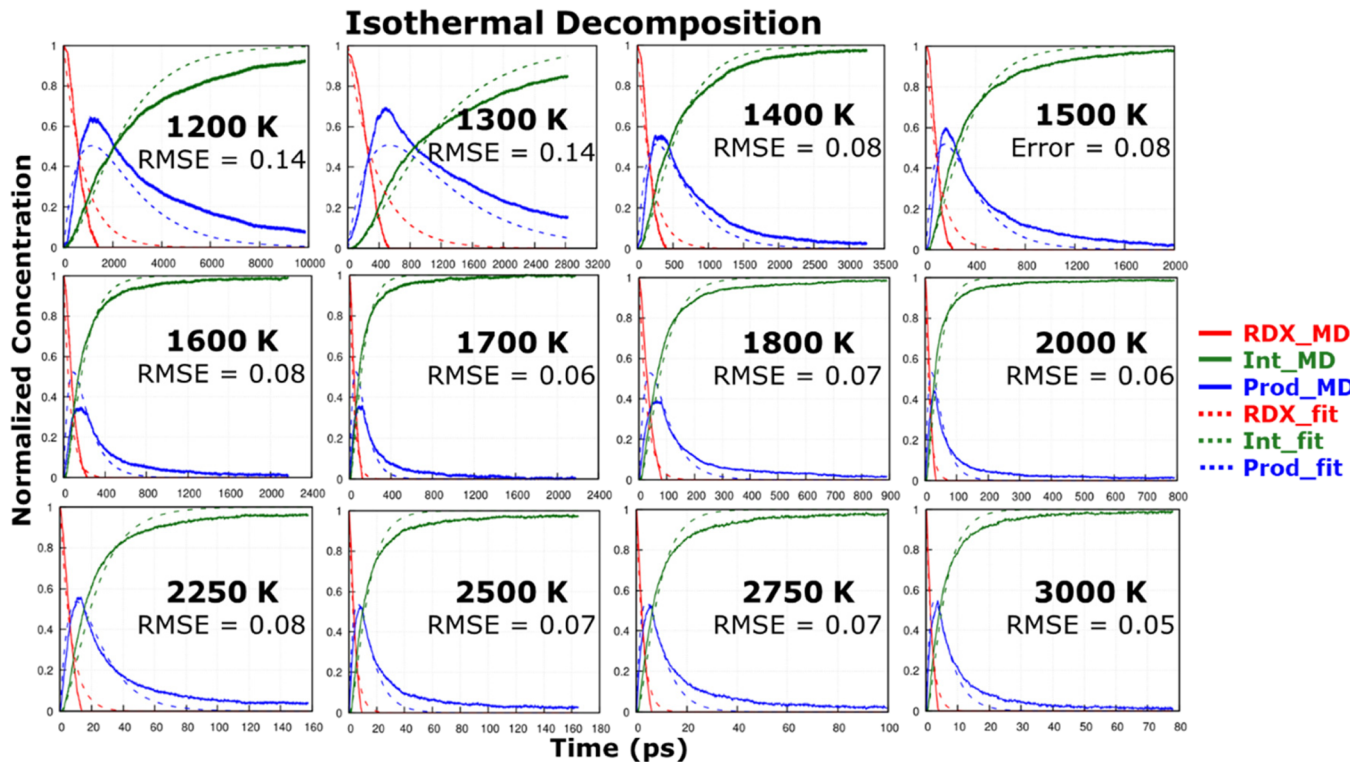


Figure 4. Calibrating species for two components + PE model between isothermal MD fit and raw data for various temperatures ranging from 1200 to 3000 K.

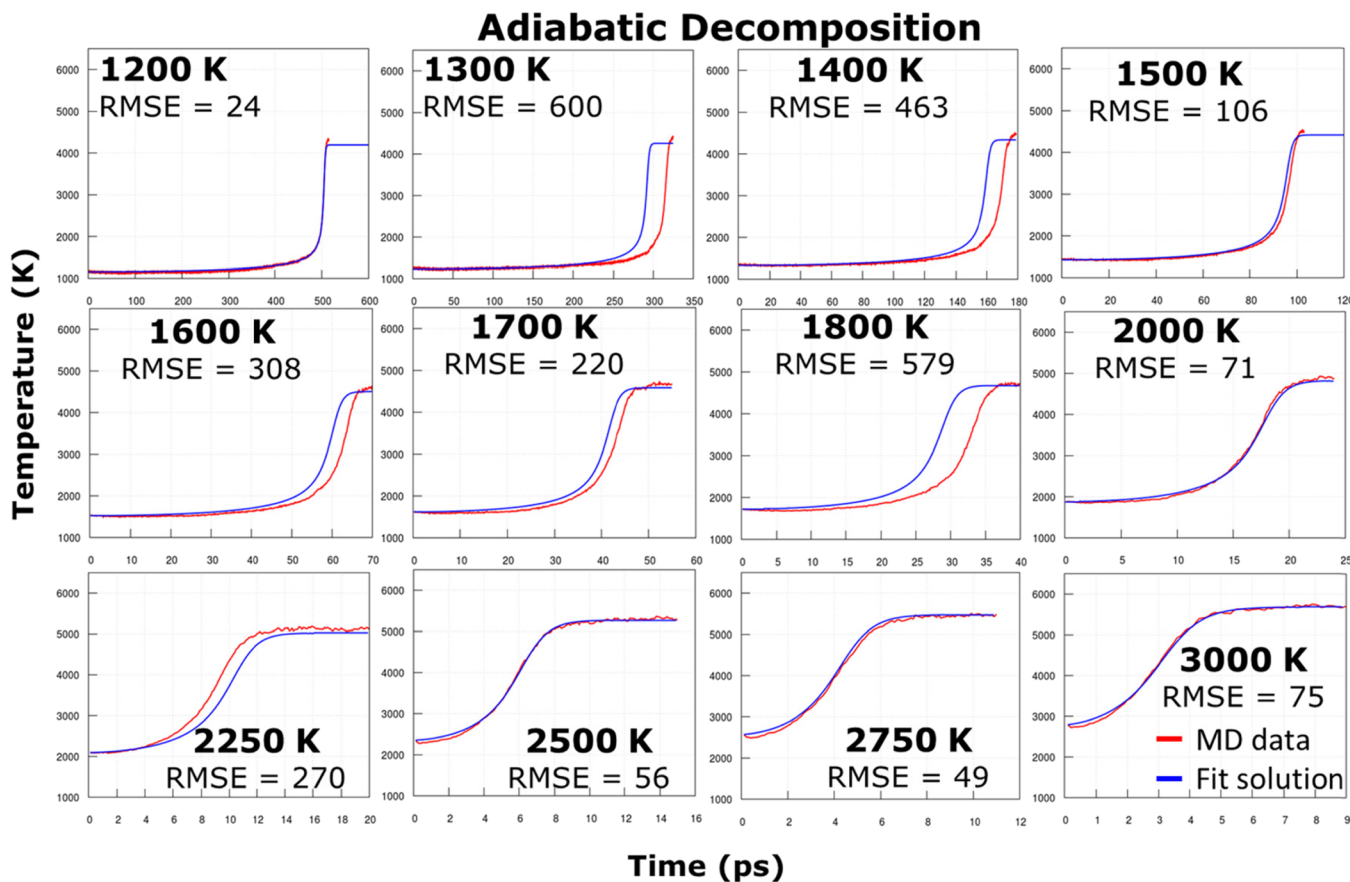


Figure 5. Calibrating heat release coefficients by comparing temperature evolution between the adiabatic MD fit using isothermal kinetics and global heats of reaction, and raw data.

especially for C_1 and C_2' , the overall trends are captured across all initial temperatures.

3.4. Heat Evolved from Adiabatic Simulations. The final piece of our reduced chemical kinetics model relates to the heat release Q_i in eq 4. These parameters could be extracted from the isothermal simulations used to parameterize the kinetics model; however, we found that doing so results in the poor description of the behavior of the system under adiabatic conditions where the positive feedback between exothermic reactions and thermally activated reactions results in quite sharp transitions and fast runaway reactions, see Figure 5. Thus, it is highly desirable to use the adiabatic simulations to parameterize the heat evolution.

We tried multiple functional forms to describe the temperature dependence of Q_1 and Q_2 (see the Supporting Information, Figure S3) and found that a piecewise or segmented linear regression model represent a good compromise between accuracy and simplicity. The parameters were obtained using a least-squares algorithm to minimize the error between the MD adiabatic temperature curve and the model (with fixed kinetics parameters described above). The values obtained from this global fit are presented in Table 2; the function curve is

Table 2. Heats of Reaction Fitted to Two Component + PE Model^{a,b}

temperature	Q_1 [kcal/mol]	Q_2 [kcal/mol]
$T \leq 1736.3$ K	-1.7 ± 0.2	416 ± 42
$T \geq 1736.3$ K	$-1.7 + 0.0314 \times (T - 1736.3) \pm 0.2 + 0.0314 \times (T - 1736.3)$	$416 - 0.03836 \times (T - 1736.3) \pm 42 - 0.03836 \times (T - 1736.3)$

^aErrors (for sensitivity analysis) in fit calculated as 10% of the computed value. ^bGlobal pair of Q_1/Q_2 parameters that replicate the adiabat potential energy curve at all temperatures was established to be the best method to reduce the RMS error.

displayed in the Supporting Information, Figure S4. We attribute the temperature dependence of Q_i to the possible energy difference between molecules belonging to the various components exhibiting different temperature dependence and from slight changes in the detailed reactions with temperature.

Figure 5 compares the prediction of the optimized model with the MD data used for parameterization. We find that the model accurately captures the adiabatic evolution of RDX under a wide range of initial conditions. The extracted heats of reaction provide interesting insight into the model. Following our notation that a positive value is exothermic, the first step can be considered as slightly endothermic at low temperatures and slightly exothermic at high temperatures, whereas the second step is highly exothermic. In these low-temperature simulations, the model captures the initial endothermic processes, though small in magnitude compared to Q_2 . These behaviors are likely associated with the loss of the crystalline order in RDX which are not observed at high temperatures.³⁸ We found capturing the low-temperature behavior, with long induction times, to be challenging. To achieve a good description, we increased the weight of the $T_0 = 1200$ K simulation by a factor of 20.

With our completed model of chemical kinetics and heat release coefficients extracted from isothermal and adiabatic simulations, we make one last verification of our parameters by comparing against MD adiabatic concentrations using a first-order Euler integrator to solve the kinetics model; see the Supporting Information for details. A comparison of the MD data and the model are shown in Figure 6. The model captures

the overall behavior of the various components accurately. In addition, we checked our model's prediction of PE evolution under adiabatic, Figure S5 of the Supporting Information, and isothermal conditions, Figure S6. Finally, we tested how well the model fits inside and outside the fitting parameter temperature range for two additional adiabatic systems; see Figure S7 of the Supporting Information. The model manages to fit the adiabatic temperature starting at $T_0 = 1250$ K because it is inside our temperature fitting range, but slightly overapproximates the timescales for complete reaction at $T_0 = 1100$ K. This justifies the need to be cautious when extrapolating beyond the fitting regime as it can be a potential cause for discrepancies between the model and data.

Figure 7 compares the characteristic timescales on our model as a function of inverse temperatures against comparable models in the literature. We show both the three NMF components and the two components + PE parameterizations, which are relatively close to each other. We note a large spread in the characteristic times across models. Our results are in good agreement with the work of Stewart⁴⁵ and Tarver et al.,²⁷ although the latter is faster than ours. We also include HMX results from Henson and Smilowitz as well as from Tarver et al.^{27,43} because they belong to the same family of nitramines and have similar decomposition pathways.⁷⁴ We find that the HMX models of Henson–Smilowitz and Tarver/Chidester/Nichols from experiments are much slower than ReaxFF-2014 for RDX.

3.5. Specific Heat for each Component. Before moving on to the continuum model, we describe the temperature-dependent specific heats for each component using eqs 1 and 2. To extract the density of states corresponding to the first component (C_1 or reactant), we used the first five picoseconds for simulations between 10 and 2000 K. Only atoms belonging to the first component were utilized. The second component (C_2 , representing intermediates) was created by using a time period where this component has a large population profile from our NMF dimensionality reduction method. Specific heat values at temperatures below 1200 K were obtained by taking the density of states at 1200 K. Finally, the third component (C_3 or products) was established from density of states calculations for simulated temperatures above 1200 K after their potential energies reached steady-state equilibrium. Again, lower temperature product specific heats were calculated assuming that the 1200 K density of states were produced at these temperatures.

We validated our model by comparing the time evolution of the total specific heat computed directly from isothermal simulations, using a sliding window of 5 ps, with the mole-fraction-weighted sum of each component's specific heat. A plot for $T = 2400$ K can be found in the Supporting Information, Figure S8. The model captures the explicit simulations very well, with the maximum difference being less than 3%. We note that the overall change in specific heat during this isothermal process is very small.

4. CONTINUUM MODEL AND HOTSPOT SIMULATIONS

4.1. Model and Implementation. We developed a continuum model to describe the coupled physics of reduced-order chemistry and thermal transport and implemented them in the MOOSE simulation framework.^{75,76} The reduced-order chemical kinetics model, as described by eqs 3aa–c, 4, and 5, is implemented and solved numerically using the finite element (FE) method within MOOSE. The parameters used in the simulations are listed in Tables 1 and 2. To account for

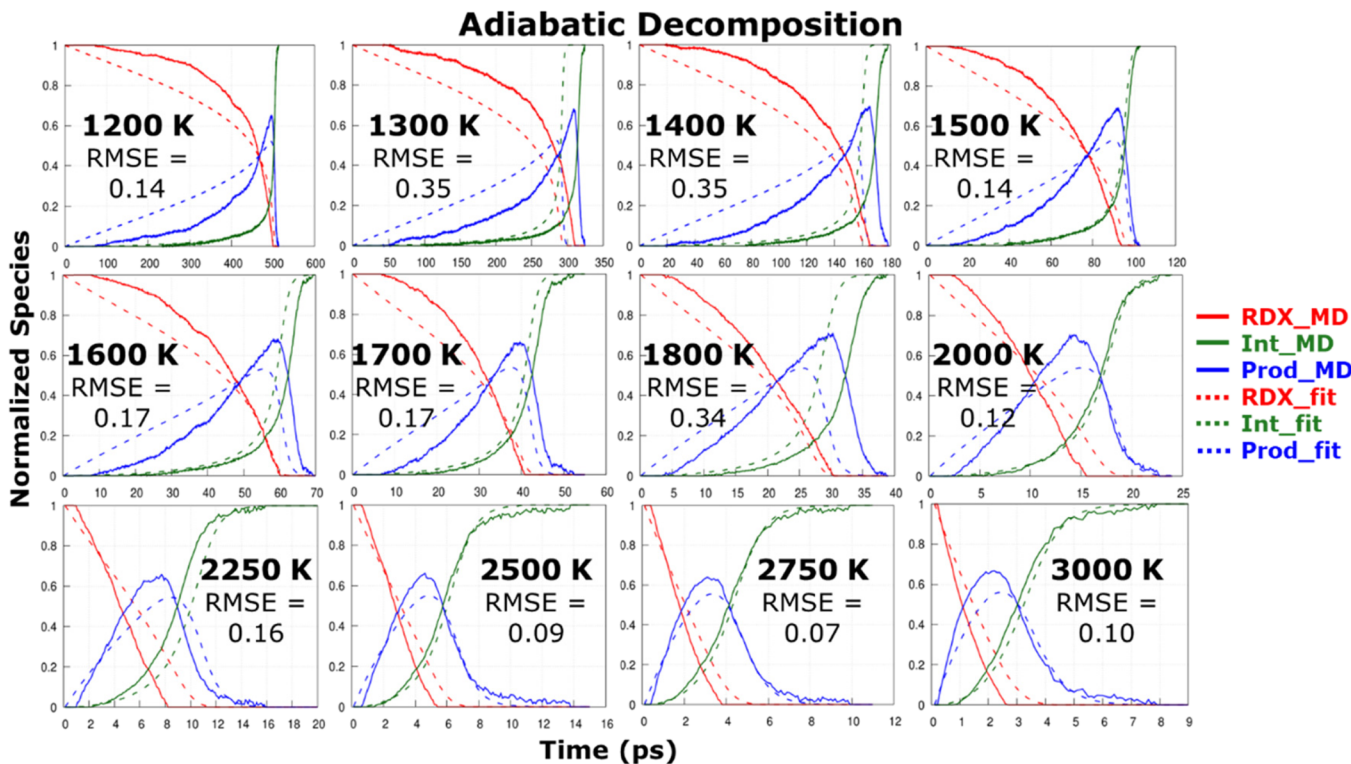


Figure 6. Evolution of the components in Figure 5, comparing concentration profiles between raw data and adiabatic MD fit using isothermal kinetics and global heats of reaction parameters.

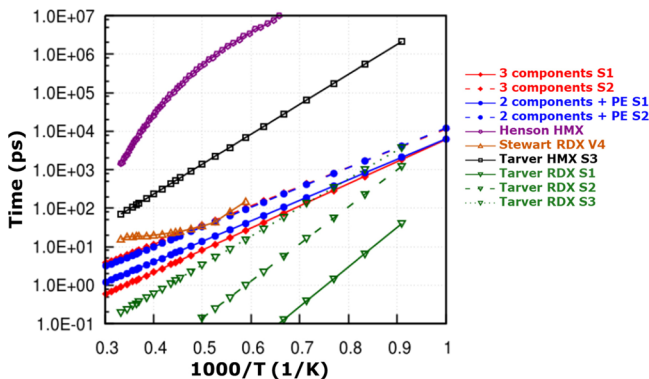


Figure 7. Characteristic times for temperatures ranging from 1000 to 3000 K comparing the two methods with the experimental data. Steeper slopes and larger y -intercepts at $T = 0$ K indicates larger activation energies and smaller prefactors, respectively. The two different MD fits are comparable to experiments in terms of timescales. Other curves were taken from refs^{27, 43, 45}.

temperature gradients, the heat diffusion term is enabled and incorporated in eq 4:

$$\rho C_v \dot{T} = k \nabla^2 T - Q_1 \dot{C}_1 + Q_2 \dot{C}_3 \quad (6)$$

The system of equations is solved simultaneously by invoking the preconditioned Jacobian-free Newton–Krylov (PJFNK) method^{76,77} along with an explicit Euler scheme for time integration.⁷⁶ For this purpose, the system of coupled partial differential equations is converted to its weak form to generate a variational statement, which is obtained using the Galerkin method of weighted residuals. This is achieved by multiplying all of the equations by a test function, ψ , and integrating all of them over the whole domain, Ω . Moreover, the divergence theorem is

applied on the heat diffusion term in conjunction with the zero heat flux boundary condition. These procedures yield the weak form of our thermochemical model:

$$\int_{\Omega} \varphi C_1 d\Omega + \int_{\Omega} \varphi C_1 Z_a \exp\left(-\frac{E_a}{RT}\right) d\Omega = 0 \quad (7a)$$

$$\begin{aligned} \int_{\Omega} \varphi C_2 d\Omega + \int_{\Omega} \varphi C_2 Z_a \exp\left(-\frac{E_a}{RT}\right) d\Omega \\ + \int_{\Omega} \varphi C_2 Z_b \exp\left(-\frac{E_b}{RT}\right) d\Omega = 0 \end{aligned} \quad (7b)$$

$$\begin{aligned} \int_{\Omega} \varphi \rho C_v T d\Omega + \int_{\Omega} \nabla \varphi \times K \nabla T d\Omega + \int_{\Omega} \varphi Q_1 C_1 d\Omega \\ - \int_{\Omega} \varphi Q_2 C_3 d\Omega = 0 \end{aligned} \quad (7c)$$

By applying the standard finite element process, the weak form is then discretized using the basis function expansion and the integrals are evaluated using the Gaussian quadrature. This leads to a system of nonlinear equations with the residual form $R \rightarrow (C \rightarrow) = 0$, where the components of the vector $C \rightarrow$ are the unknowns, i.e., C_1 , C_2 , and T . With its good convergence properties, Newton's method can be employed to find the roots that minimize the residuals iteratively. However, it requires calculating and storing the Jacobian matrix explicitly at each iteration. For example, the $(n+1)$ th iterate of the vector of the unknowns is updated according to $\vec{J}(\vec{C}^n)[\vec{C}^{n+1} - \vec{C}^n] = -\vec{R}(\vec{C}^n)$, with the elements of the Jacobian matrix given by $J_{ij}(\vec{C}^n) = \frac{\partial R_i(\vec{C}^n)}{\partial C_j}$. To alleviate this requirement and hence reduce computational cost and reduce memory footprint, the

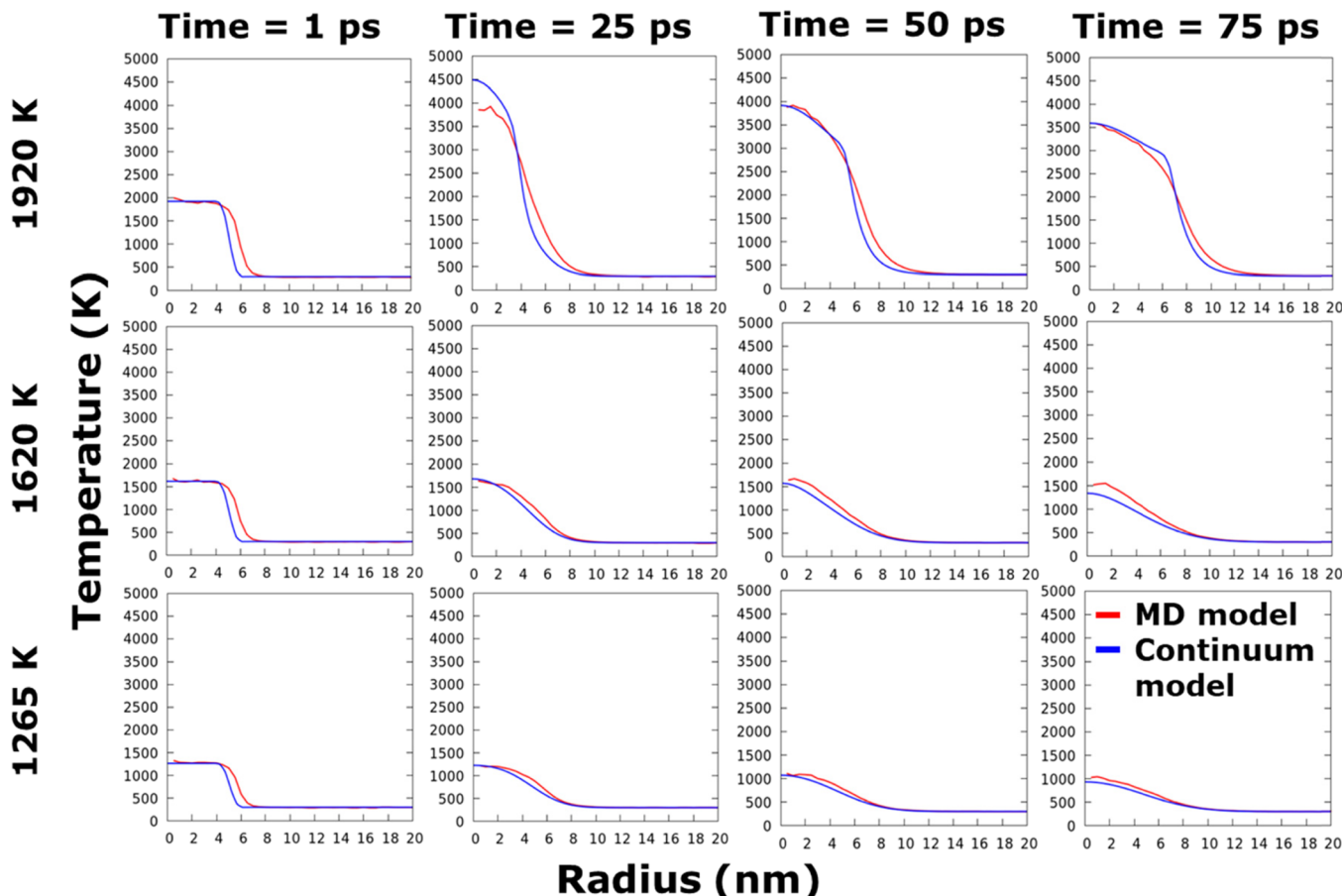


Figure 8. Snapshots for 10 nm hotspot in diameter seeded to 1920 K (both critical), 1620 K (both quench), and 1265 K (both quench). The model reacts slightly faster compared to the 1920 K MD hotspot at 25 ps due to the volume relaxation and formation of the reaction zone. Lastly, when both the MD and continuum model quench, they have similar profiles.

PJFNK method employs the iterative Krylov algorithm to produce a sequence of iterates in the Krylov subspace for each nonlinear iteration of the Newton algorithm. For PJFNK to be efficient, a preconditioning matrix is usually needed. The preconditioning matrix is built using the Single Matrix Preconditioner (SMP) option and the automatic differentiation capability available in the MOOSE framework.⁷⁶

4.2. Simulation Details. The hotspot is represented by a circular region with diameter d (ranging from 10 nm to 1 μm) located at the center of a square domain with side $3d$. The dimension of the system is chosen to be large enough that it does not affect the transients within the hotspot. Smaller simulation cells, matching the size of the MD simulations, were also conducted and show negligible differences. The initial temperature of the hotspot is T_0 , and the temperature of remaining domain is 300 K. A constant timestep size of 0.1 ps and a mesh spacing of 0.333 nm are used for the smaller hotspot simulations. For the micron-size hotspot, a coarser square mesh is used with an element size of 2.5 nm. In addition, the system is assumed to be closed; i.e., there is no heat or mass exchange with the surroundings. No mechanical work is considered in these hotspot simulations.

In Section 5, to validate our model by making meaningful comparisons with the MD simulations regarding hotspot criticality,³⁸ we use a thermal conductivity $k = 0.361 \frac{\text{W}}{\text{m} \cdot \text{K}}$, which corresponds to a system size of 30 nm from Section 2.2, as well as a classical specific heat. Later in Section 6.2, we discuss

the effects that length-dependent thermal conductivity and an accurate specific heat accounting for quantum mechanical effects have on altering our predictions for hotspot criticality.

5. MODEL VALIDATION: NANOSCALE HOTSPOT EVOLUTION

To validate our atomistically informed continuum model, we studied the criticality of nanoscale hotspots and compared the model predictions with explicit MD simulations. The evolution of a hotspot is governed by a complex interplay between thermal diffusion and chemical reactions. For temperatures below a critical value (that depends of size and geometry), thermal transport and initial endothermic reactions conspire to quench the hotspot. However, if the temperature is high enough, exothermic reactions will overtake the system and the hotspot will result in a self-propagating deflagration wave.

Figure 8 shows the temperature profiles of cylindrical hotspots at various times and for three initial temperatures. The hotspots are cylindrical with axis along the [001] direction and a diameter of 10 nm; they are initialized with temperatures between 1500 and 2500 K. For both the MD and FE simulations we apply adiabatic conditions and follow the temporal evolution of the system. The details of the MD simulations can be found in ref 38. The continuum model uses a classical specific heat to enable comparisons with the MD simulations. We find very similar qualitative and quantitative behaviors between the atomistic and continuum models at all temperatures and times explored. The

1920 K hotspot turns into a deflagration wave in both models; running to longer times showed a core temperature of roughly 3000 K and expansion of the reaction front. On the other hand, the 1620 and 1265 K hotspots were subcritical; both the continuum model and the MD data show the quenching of the core. A minor difference between the models is the slight overestimation of temperature at early times by the continuum model for our 1920 K hotspot, see the profile at 25 ps. Further examination of the concentration profiles indicate that this is roughly the time when the reaction zone forms. In the MD simulation, we see a very obvious decrease in the density due to the formation of intermediates and product gases within the core. This causes volume expansion and mass transport. However, in these simulations, the continuum model is not coupled to equations of state or mechanics; hence, no volume relaxation is considered. The lack of mechanical work results in a slightly higher temperature in the core. However, we see that at later times, the maximum temperature of the core approximately matches the value obtained from MD; hence, we believe the model appropriately captures the key features of the MD hotspot in both critical and quench situations.

6. HOTSPOT CRITICALITY AND UNCERTAINTY QUANTIFICATION

6.1. Critical Temperature as a Function of Size. Having verified the accuracy of the continuum model for 10 nm diameter hotspots, the next step is to scale up the simulations beyond the capabilities of the MD. We modeled the hotspots of sizes between 10 nm and 1 μm in diameter and obtain critical hotspot temperatures. To identify the critical temperature for each hotspot size, simulations with various initial temperatures (in increments of 10 K) were carried out, and the temporal evolution of the hotspot temperature was analyzed. The criterion used to define the critical temperature is taken as the minimum initial temperature for which hotspot ignition occurs, leading to a deflagration wave that propagates through the system. In general, this distinction between critical and subcritical hotspots was clear, with a well-defined critical temperature. It was characterized by a dramatic increase in the hotspot temperature due to the local progress of chemical decomposition in extent. This contrasts with the behavior observed in the simulation with initial temperature just below this critical temperature, for which the hotspot quenches before any appreciable progress in chemical reaction and the whole system eventually reaches thermal equilibrium (with final temperatures ranging between 400 and 600 K due to the adiabatic boundary conditions). If these subcritical systems are evolved for significantly longer timescales, we observe homogenous decomposition in the form of slow cook-off reactions. This is due to the use of adiabatic conditions in relatively small cells and occurs at a completely different timescale and is not of interest to ignition and growthlike models. The only exception to this criticality phenomenon was observed in the largest hotspot, 1 μm , for which the distinction between the critical and subcritical behavior is not abrupt. For instance, none of the simulations with initial temperatures above 700 K quenched significantly; thus in all cases, we observed ignition at varying induction times, followed by the propagation of a combustion wave. Possible reasons for this larger length-scale behavior will be discussed in the following subsection. As a result, a different criterion was employed to determine the critical temperature of the 1 μm hotspot: the induction time was

not to exceed 50 ns. This was chosen to be similar to the 1-D time-to-explosion observed experimentally, see ref 27.

Figure 9 shows the critical hotspot temperature as a function of diameter for our model and includes the results from Tarver et

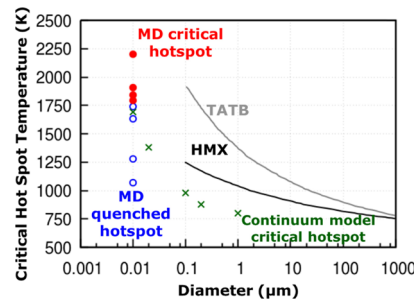


Figure 9. Hotspot temperature vs critical hotspot size from both MD simulations and continuum model for RDX. Data from MD for 10 nm hotspot in diameter shows that the model can capture critical temperature. Classical specific heat used, and thermal conductivity taken as the low value as it is close to experiments. Values for HMX and TATB obtained from Tarver et al. *J. Phys. Chem.* 1996.²⁷

al. ignition and growth model for HMX and TATB.²⁷ We also show MD results for a 10 nm hotspot for completeness. In these continuum simulations, we use a quantum mechanical specific heat and thermal conductivity value associated with a length of a 30 nm sample as stated above. The results indicate that the critical hotspot temperature for our RDX model is comparable to, but slightly lower than, the HMX model of Tarver et al. This is interesting because HMX and RDX are similar nitramines and are believed to have similar kinetics. We stress that our model is based on reactive MD simulations and includes uncertainties associated with it, while the HMX model is derived from experiments. We consider these results to be very promising as they indicate the real possibility of predictive multiscale models for HE materials.

6.2. Role of Heat Transport, Specific Heat, and Reduced Chemistry Model on Hotspot Criticality. As in any physics-based modeling that involves calibration, there are uncertainties associated with both the model form and its parameters. The uncertainties in model parameters have disparate origins, and we discussed some of the model-form errors associated with the reduced chemical kinetics model in Section 3. There are intrinsic uncertainties in the MD simulations that are associated with the interatomic potential and with the use of classical (as opposed to quantum) dynamics. Recent work has explored how details of the force field use affects predictions in energetic materials^{73,78} and the effect of quantum effects on dynamics are beginning to be explored.³⁹ The mathematical form of the reduced order model also introduces uncertainties. In addition, there are uncertainties associated with the simulation setup, statistical fluctuations, and the numerical errors during the fitting procedure. A full characterization of uncertainties is beyond the scope of this paper;⁷⁹ here, we quantify how the parameters in the continuum model affect critical temperatures. We considered the specific heat capacity, thermal conductivity, reaction rates, and heat of reaction. Figure 10 shows how each independently perturbed model parameter affects the critical temperature versus size curves. The nominal simulations use the following: temperature-dependent specific heat, bulk thermal conductivity, and the reported average values of kinetics and heat release.

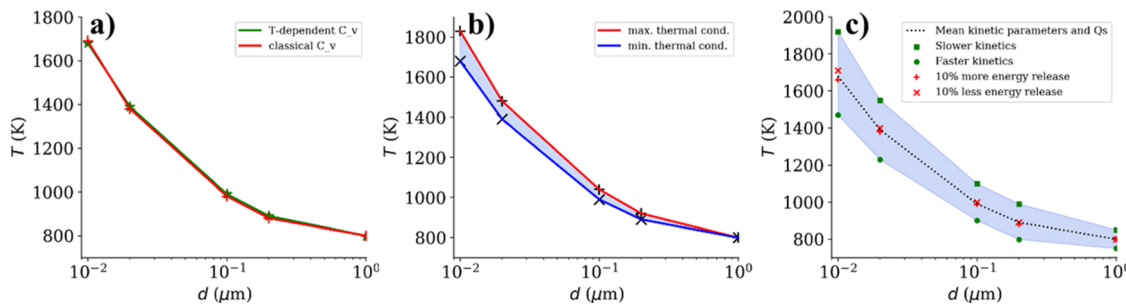


Figure 10. Sensitivity of the predicted critical hotspot temperature (as a function of hotspot diameter d) to uncertainty in the continuum model parameters: (a) impact of using quantum-corrected vs classical specific heat, (b) size-dependent thermal conductivity: comparing $k_{\min} = 0.361 \frac{\text{W}}{\text{m} \cdot \text{K}}$ with bulk thermal conductivity of $0.595 \frac{\text{W}}{\text{m} \cdot \text{K}}$, and (c) effects of uncertainty in kinetics parameters and heat of reactions.

For specific heat capacity, simulations using the temperature-independent classical limit are compared with those using the temperature-dependent form presented in Section 2.2, which takes quantum statistical mechanics into consideration. The classical value used was $0.563 \frac{\text{cal}}{\text{g} \cdot \text{K}}$, as compared to a function of temperature that increases from 0 at $T = 0 \text{ K}$ to $0.54 \frac{\text{cal}}{\text{g} \cdot \text{K}}$ for temperatures above 2600 K, previously computed and validated in Section 3.5. Figure 10(a) shows that the quantum-correction to the isochoric specific heat capacity results in a relatively small change in the critical temperature for all hotspot sizes considered. The reason behind this behavior will be further clarified but while we find that a classical specific heat does affect the final temperature achieved, this change in temperature is not sufficient to significantly affect the transition to deflagration.

To assess the effect of thermal conductivity on hotspot criticality, we compare the results ranging from an upper limit of $0.595 \frac{\text{W}}{\text{m} \cdot \text{K}}$, corresponding to a bulk sample, to a lower limit of $0.361 \frac{\text{W}}{\text{m} \cdot \text{K}}$, corresponding to a system size of 30 nm. Figure 10b shows that the sensitivity to thermal conductivity is higher for nanoscale hotspots than larger ones. This indicates that thermal transport has a stronger effect on smaller hotspots, and that the large surface to volume ratio results in faster cooling.

Figure 10c quantifies uncertainties in the heats of reaction by varying Q_1 and Q_2 by plus and minus 10%. The values in Table 2 as a function of temperature were multiplied by 1.1 and 0.9 for more and less energy released in each step, respectively. Interestingly, perturbing the heat of reactions played a minimal role in determining the critical temperature regardless of size. What is affected by changing the heat evolved variables is, as expected, the final temperature following the complete reaction.

Finally, we examine the sensitivity in the kinetics model, summarized in Table 1, by using one standard deviation (to be called here σ) as an estimate of the upper and lower limits of the kinetics rates. We created *slow* and *fast* kinetics models corresponding to the set of kinetics parameters that makes each reaction step the slowest or the fastest. For example, the i th step in the fast model will have a rate with a prefactor set equal to $\ln(Z_i + \sigma)$ and activation energy given by $E_i - \sigma$. This results in the fastest kinetics having values $\ln(Z_a) = 31.5 \ln(\text{s}^{-1})$, $E_a = 22.9 \text{ kcal/mol}$, $\ln(Z_b) = 30.5 \ln(\text{s}^{-1})$, and $E_b = 21.9 \text{ kcal/mol}$, compared to the slowest kinetics having values $\ln(Z_a) = 29.7 \ln(\text{s}^{-1})$, $E_a = 25.9 \text{ kcal/mol}$, $\ln(Z_b) = 28.7 \ln(\text{s}^{-1})$, and $E_b = 25.1 \text{ kcal/mol}$. As is evident in Figure 10c, variations in the kinetics model has a much stronger effect in smaller hotspots and their role decreases with size. For a 10 nm hotspot, the range of critical

temperature varies between 1470 and 1820 K, whereas the 1 μm hotspot results in a narrower range of 780 to 910 K.

To better understand these trends, we need to address first the factors that control the criticality of the hotspot. Criticality requires that the thermal energy be retained in the hotspot core for a long enough time to reach ignition. In our thermochemical model, the competing mechanism that can prevent the system from reaching the ignition phase is the thermal diffusion. Hence, a rough estimate can be made to derive the criticality condition in a closed system, assuming that the temperature change due to chemical reactions within the induction stage is negligible. This condition dictates that the induction time should be smaller than the thermalization time (the time constant for temperature gradients to disappear). It is well known that the thermalization time increases with hotspot size and decreasing thermal diffusivity. For example, Phillip⁸⁰ used the analytical solution of the heat diffusion equation with no heat sources to show that the characteristic time to cool down a hot sphere in a direct contact with an infinite solid medium of the same thermal properties is inversely proportional to thermal diffusivity, while linearly proportional to the square of the sphere diameter. Thus, the criticality of smaller hotspots can be expected to be more sensitive to thermal conductivity, where the thermal diffusion kinetics competes strongly with the chemical reaction kinetics. Unlike the smaller hotspots, at the micron level, the thermal quenching is slow enough that the reaction rates are controlled by the kinetics and initial temperature. Thus, the critical temperature becomes less dependent on the hotspot diameter.

We now discuss the weak dependence of critical temperature on specific heat. For this purpose, the temporal evolution of the average temperature across the entire sample is shown in Figure 11 for the 10 nm and 1 μm hotspots. For each size, we show the results from two different initial temperatures (one of them is the critical temperature) and classical and quantum specific heats. This shows that the transients as well as the steady-state temperature obtained from the two different forms of the specific heat are significantly different. As expected, the reaction time is smaller and the temperature is higher in the quantum-corrected case. Yet, these changes are not sufficient to significantly affect the transition to deflagration.

7. CONCLUSIONS

We developed a multiscale model to describe chemistry and thermal transport in RDX from molecular dynamics simulation and used it to assess the criticality of thermal hotspots. We used unsupervised learning via the non-negative matrix factorization technique to coarse grain the detailed chemistry in the reactive

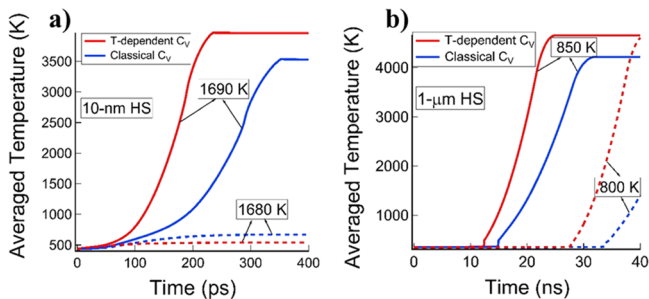


Figure 11. Temporal evolution of the averaged temperature for an RDX system due to the decomposition of a hotspot with an initial temperature T_0 . Hotspot sizes 10 nm (a) and 1 μm (b) are shown using the quantum-corrected and classical specific heat. Two different initial temperatures are illustrated for each hotspot size.

MD simulations to three components that represent reactants, intermediates, and final products. We proposed kinetics equations to describe the time evolution of the components and parameterize the model to minimize the errors between our model and MD data to obtain global kinetics. We parameterized the model from reactive MD simulations under two different conditions: (i) kinetics constants were obtained from homogeneous isothermal decomposition simulations and (ii) heat of reaction coefficients were obtained from adiabatic simulations. In addition, thermal conductivity and specific heat were obtained from MD. In this work, the number of components used in the kinetics model was determined by analyzing the accuracy of the dimensionality reduction step, without input from the resulting kinetics model. Future work should explore determining the number of components based on the accuracy of the resulting kinetics model and/or the use of machine learning tools to learn the dimensionality reduction and kinetics model at the same time.

We used the continuum model to characterize the evolution of hotspots in RDX. The multiscale model was validated by comparing its predictions with explicit MD simulations for the time evolution of nanoscale hotspots. We find good agreement in the evolution of temperature profiles, both for initial temperatures where the hotspot quenches and those under which a deflagration wave develops. This constitutes an important validation as the model has only been parameterized with homogeneous MD simulations.

The continuum model was then used to span different hotspot sizes and determine criticality; comparisons were made with the Tarver/Chidester/Nichols Ignition and Growth model. For the largest hotspot size studied (with a diameter of 1 μm), the predicted critical temperature for ignition of RDX was found to be smaller than the calculated values for HMX and TATB, reported by Tarver et al. We investigated the sensitivity of our model prediction to the uncertainties in the MD calibrated parameters, namely, kinetics, heats of reaction, size-dependent thermal conductivity, and quantum effects on specific heat capacity. Among all of these parameters, uncertainty in the kinetics parameters of our Arrhenius model is the most influential ingredient. Future work on exploring more components using different reaction schemes as well as implementing pressure and density effects should be pursued.

ASSOCIATED CONTENT

S Supporting Information

The Supporting Information is available free of charge at <https://pubs.acs.org/doi/10.1021/acs.jPCA.0c07320>.

Further details regarding the extraction of the necessary parameters from the MD simulations, as well as comparisons of the model with the raw data: (i) simulation tool for extracting a three-component fit from our reactive MD simulation, (ii) algorithm for extracting kinetics parameters given multiple three-component curves based on Arrhenius kinetics, (iii) RMSE equation for each number of component and temperature pair combination, (iv) RMSE equation for the three-component raw MD data and the kinetics model, (v) comparisons of isothermal and adiabatic concentrations, (vi) different fitting forms for the heat evolved and algorithm for extracting and comparing the heats of reaction, and (vii) specific heat functional form comparing the sum of components to the values obtained from MD ([PDF](#))

AUTHOR INFORMATION

Corresponding Author

Alejandro Strachan – School of Materials Engineering and Birck Nanotechnology Center, Purdue University, West Lafayette, Indiana 47907, United States; Email: strachan@purdue.edu

Authors

Michael N. Sakano – School of Materials Engineering and Birck Nanotechnology Center, Purdue University, West Lafayette, Indiana 47907, United States; orcid.org/0000-0003-3337-4810

Ahmed Hamed – School of Mechanical Engineering, Purdue University, West Lafayette, Indiana 47907, United States

Edward M. Kober – Theoretical Division, Los Alamos National Laboratory, Los Alamos, New Mexico 87545, United States

Nicolo Grilli – Department of Engineering Science, University of Oxford, OX1 3PJ Oxford, United Kingdom

Brenden W. Hamilton – School of Materials Engineering and Birck Nanotechnology Center, Purdue University, West Lafayette, Indiana 47907, United States; orcid.org/0000-0002-4524-2201

Md Mahbubul Islam – Department of Mechanical Engineering, Wayne State University, Detroit, Michigan 48202, United States

Marisol Koslowski – School of Mechanical Engineering, Purdue University, West Lafayette, Indiana 47907, United States

Complete contact information is available at:

<https://pubs.acs.org/10.1021/acs.jPCA.0c07320>

Notes

The authors declare no competing financial interest.

ACKNOWLEDGMENTS

This work was primarily supported by the US Office of Naval Research, Multidisciplinary University Research Initiatives (MURI) Program, Contract: N00014-16-1-2557. Program managers: Chad Stoltz and Kenny Lipkowitz. E.M.K. was supported through the High Explosives Grand Challenge program at the Los Alamos National Laboratory (Program Manager: Dan Borovina).

■ REFERENCES

- (1) Davis, W. C. High explosives: The interaction of chemistry and mechanics. *Los Alamos Science* **1981**, 48–75.
- (2) Field, J. E. Hot spot ignition mechanisms for explosives. *Acc. Chem. Res.* **1992**, 25, 489–496.
- (3) Handley, C. A.; Lambourn, B. D.; Whitworth, N. J.; James, H. R.; Belfield, W. J. Understanding the shock and detonation response of high explosives at the continuum and meso scales. *Appl. Phys. Rev.* **2018**, 5, No. 011303.
- (4) Gustavsen, R. L.; Sheffield, S. A.; Alcon, R. R. Measurements of shock initiation in the tri-amino-tri-nitro-benzene based explosive PBX 9502: Wave forms from embedded gauges and comparison of four different material lots. *J. Appl. Phys.* **2006**, 99, 114907.
- (5) Burns, M. J.; Gustavsen, R. L.; Bartram, B. D. One-dimensional plate impact experiments on the cyclotetramethylene tetranitrime (HMX) based explosive EDC32. *J. Appl. Phys.* **2012**, 112, No. 064910.
- (6) Garcia, F.; Vandersall, K. S.; Tarver, C. M. Shock initiation experiments with ignition and growth modeling on low density HMX. *J. Phys. Conf. Ser.* **2014**, 500, No. 052048.
- (7) Lee, E. L.; Tarver, C. M. Phenomenological model of shock initiation in heterogeneous explosives. *Phys. Fluids* **1980**, 23, 2362–2372.
- (8) Johnson, J. N.; Tang, P. K.; Forest, C. A. Shock-wave initiation of heterogeneous reactive solids. *J. Appl. Phys.* **1985**, 57, 4323–4334.
- (9) Wescott, B. L.; Stewart, D. S.; Davis, W. C. Equation of state and reaction rate for condensed-phase explosives. *J. Appl. Phys.* **2005**, 98, No. 053514.
- (10) Nichols, A. L. Statistical Hot Spot Model for Explosive Detonation. *AIP Conf. Proc.* **2006**, 845, 465–470.
- (11) Hill, L. G.; Zimmermann, B.; Nichols, A. L. On the burn topology of hot-spot-initiated reactions. *AIP Conf. Proc.* **2009**, 1195, 432–435.
- (12) Hill, L. G. The shock-triggered statistical hot spot model. *AIP Conf. Proc.* **2012**, 1426, 307–310.
- (13) Menikoff, R.; Shaw, M. S. The SURF model and the curvature effect for PBX 9502. *Combust. Theory Model.* **2012**, 16, 1140–1169.
- (14) Aslam, T. D. Shock temperature dependent rate law for plastic bonded explosives. *J. Appl. Phys.* **2018**, 123, 145901.
- (15) Lee, S.; et al. Effects of parametric uncertainty on multi-scale model predictions of shock response of a pressed energetic material. *J. Appl. Phys.* **2019**, 125, 235104.
- (16) Austin, R. A.; Barton, N. R.; Reaugh, J. E.; Fried, L. E. Direct numerical simulation of shear localization and decomposition reactions in shock-loaded HMX crystal. *J. Appl. Phys.* **2015**, 117, 185902.
- (17) Rai, N. K.; Schmidt, M. J.; Udaykumar, H. S. Collapse of elongated voids in porous energetic materials: Effects of void orientation and aspect ratio on initiation. *Phys. Rev. Fluids* **2017**, 2, No. 043201.
- (18) Wood, M. A.; Kittell, D. E.; Yarrington, C. D.; Thompson, A. P. Multiscale modeling of shock wave localization in porous energetic material. *Phys. Rev. B* **2018**, 97, No. 014109.
- (19) Rai, N. K.; Udaykumar, H. S. Void collapse generated meso-scale energy localization in shocked energetic materials: Non-dimensional parameters, regimes, and criticality of hotspots. *Phys. Fluids* **2019**, 31, No. 016103.
- (20) Duarte, C. A.; et al. Void Collapse in Shocked -HMX Single Crystals: Simulations and Experiments. *Propellants, Explos., Pyrotech.* **2020**, 45, 243–253.
- (21) Sen, O.; Rai, N. K.; Diggs, A. S.; Hardin, D. B.; Udaykumar, H. S. Multi-scale shock-to-detonation simulation of pressed energetic material: A meso-informed ignition and growth model. *J. Appl. Phys.* **2018**, 124, No. 085110.
- (22) Miller, C.; Kittell, D.; Yarrington, C.; Zhou, M. Prediction of Probabilistic Detonation Threshold via Millimeter-Scale Microstructure-Explicit and Void-Explicit Simulations. *Propellants, Explos., Pyrotech.* **2020**, 45, 254–269.
- (23) Shan, T.-R.; Thompson, A. P. Shock-induced hotspot formation and chemical reaction initiation in PETN containing a spherical void. *J. Phys. Conf. Ser.* **2014**, 500, 172009.
- (24) Wood, M. A.; Cherukara, M. J.; Kober, E. M.; Strachan, A. Ultrafast Chemistry under Nonequilibrium Conditions and the Shock to Deflagration Transition at the Nanoscale. *J. Phys. Chem. C* **2015**, 119, 22008–22015.
- (25) Bassett, W. P.; Johnson, B. P.; Salvati, L.; Dlott, D. D. Hot-spot generation and growth in shocked plastic-bonded explosives studied by optical pyrometry. *J. Appl. Phys.* **2019**, 125, 215904.
- (26) Li, C.; Hamilton, B. W.; Strachan, A. Hotspot formation due to shock-induced pore collapse in 1,3,5,7-tetranitro-1,3,5,7-tetrazocane (HMX): Role of pore shape and shock strength in collapse mechanism and temperature. *J. Appl. Phys.* **2020**, 127, 175902.
- (27) Tarver, C. M.; Chidester, S. K.; Nichols, A. L. Critical Conditions for Impact- and Shock-Induced Hot Spots in Solid Explosives. *J. Phys. Chem.* **1996**, 100, 5794–5799.
- (28) Chakraborty, D.; Muller, R. P.; Dasgupta, S.; Goddard, W. A. The Mechanism for Unimolecular Decomposition of RDX (1,3,5-Trinitro-1,3,5-triazine), an ab Initio Study. *J. Phys. Chem. A* **2000**, 104, 2261–2272.
- (29) Chakraborty, D.; Muller, R. P.; Dasgupta, S.; Goddard, W. A. Mechanism for Unimolecular Decomposition of HMX (1,3,5,7-Tetranitro-1,3,5,7-tetrazocine), an ab Initio Study. *J. Phys. Chem. A* **2001**, 105, 1302–1314.
- (30) Manaa, M. R.; Fried, L. E.; Melius, C. F.; Elstner, M.; Frauenheim, T. Decomposition of HMX at Extreme Conditions: A Molecular Dynamics Simulation. *J. Phys. Chem. A* **2002**, 106, 9024–9029.
- (31) Strachan, A.; Kober, E. M.; van Duin, A. C. T.; Oxgaard, J.; Goddard, W. A. Thermal decomposition of RDX from reactive molecular dynamics. *J. Chem. Phys.* **2005**, 122, No. 054502.
- (32) Strachan, A.; van Duin, A. C. T.; Chakraborty, D.; Dasgupta, S.; Goddard, W. A. Shock Waves in High-Energy Materials: The Initial Chemical Events in Nitramine RDX. *Phys. Rev. Lett.* **2003**, 91, No. 098301.
- (33) Schweigert, I. V. Ab Initio Molecular Dynamics of High-Temperature Unimolecular Dissociation of Gas-Phase RDX and Its Dissociation Products. *J. Phys. Chem. A* **2015**, 119, 2747–2759.
- (34) Perriot, R.; Negre, C. F. A.; McGrane, S. D.; Cawkwell, M. J. Density functional tight binding calculations for the simulation of shocked nitromethane with LATTE-LAMMPS. *AIP Conf. Proc.* **2018**, 1979, No. 050014.
- (35) Cawkwell, M. J.; Manner, V. W. Ranking the Drop-Weight Impact Sensitivity of Common Explosives Using Arrhenius Chemical Rates Computed from Quantum Molecular Dynamics Simulations. *J. Phys. Chem. A* **2020**, 124, 74–81.
- (36) Jaramillo, E.; Sewell, T. D.; Strachan, A. Atomic-level view of inelastic deformation in a shock loaded molecular crystal. *Phys. Rev. B* **2007**, 76, No. 064112.
- (37) Holian, B. L.; Germann, T. C.; Maillet, J.-B.; White, C. T. Atomistic Mechanism for Hot Spot Initiation. *Phys. Rev. Lett.* **2002**, 89, 285501.
- (38) Sakano, M.; Hamilton, B.; Islam, M. M.; Strachan, A. Role of Molecular Disorder on the Reactivity of RDX. *J. Phys. Chem. C* **2018**, 122, 27032–27043.
- (39) Hamilton, B. W.; Kroonblawd, M. P.; Islam, M. M.; Strachan, A. Sensitivity of the Shock Initiation Threshold of 1,3,5-Triamino-2,4,6-trinitrobenzene (TATB) to Nuclear Quantum Effects. *J. Phys. Chem. C* **2019**, 123, 21969–21981.
- (40) Islam, M. M.; Strachan, A. Decomposition and Reaction of Polyvinyl Nitrate under Shock and Thermal Loading: A ReaxFF Reactive Molecular Dynamics Study. *J. Phys. Chem. C* **2017**, 121, 22452–22464.
- (41) McGrane, S.; Bowlan, P.; Powell, M.; Brown, K.; Bolme, C. Broadband mid-infrared measurements for shock-induced chemistry. *AIP Conf. Proc.* **2018**, 1979, 130004.
- (42) Islam, M. M.; Strachan, A. Reactive Molecular Dynamics Simulations to Investigate the Shock Response of Liquid Nitromethane. *J. Phys. Chem. C* **2019**, 123, 2613–2626.

- (43) Henson, B. F.; Asay, B. W.; Smilowitz, L. B.; Dickson, P. M. Ignition Chemistry in HMX from Thermal Explosion to Detonation. *AIP Conf. Proc.* **2002**, *620*, 1069–1072.
- (44) Maillet, J.-B.; Bourasseau, E.; Desbiens, N.; Vallverdu, G.; Stoltz, G. Mesoscopic simulations of shock-to-detonation transition in reactive liquid high explosive. *EPL Europhys. Lett.* **2011**, *96*, 68007.
- (45) Lee, K.; Joshi, K.; Chaudhuri, S.; Stewart, D. S. Mirrored continuum and molecular scale simulations of the ignition of high-pressure phases of RDX. *J. Chem. Phys.* **2016**, *144*, 184111.
- (46) Luscher, D. J.; Addessio, F. L.; Cawkwell, M. J.; Ramos, K. J. A dislocation density-based continuum model of the anisotropic shock response of single crystal α -cyclotrimethylene trinitramine. *J. Mech. Phys. Solids* **2017**, *98*, 63–86.
- (47) Springer, H. K.; Bastea, S.; Nichols, A. L.; Tarver, C. M.; Reaugh, J. E. Modeling The Effects of Shock Pressure and Pore Morphology on Hot Spot Mechanisms in HMX. *Propellants, Explos., Pyrotech.* **2018**, *43*, 805–817.
- (48) Grilli, N.; Koslowski, M. The effect of crystal orientation on shock loading of single crystal energetic materials. *Comput. Mater. Sci.* **2018**, *155*, 235–245.
- (49) Duarte, C. A.; Grilli, N.; Koslowski, M. Effect of initial damage variability on hot-spot nucleation in energetic materials. *J. Appl. Phys.* **2018**, *124*, No. 025104.
- (50) van Duin, A. C. T.; Dasgupta, S.; Lorant, F.; Goddard, W. A. ReaxFF: A Reactive Force Field for Hydrocarbons. *J. Phys. Chem. A* **2001**, *105*, 9396–9409.
- (51) Wood, M. A.; van Duin, A. C. T.; Strachan, A. Coupled Thermal and Electromagnetic Induced Decomposition in the Molecular Explosive α HMX; A Reactive Molecular Dynamics Study. *J. Phys. Chem. A* **2014**, *118*, 885–895.
- (52) Plimpton, S. Fast Parallel Algorithms for Short-Range Molecular Dynamics. *J. Comput. Phys.* **1995**, *117*, 1–19.
- (53) Hakey, P.; Ouellette, W.; Zubieta, J.; Korter, T. Redetermination of cyclo-trimethyl-ene-trinitramine. *Acta Crystallogr. Sect. E Struct. Rep. Online* **2008**, *64*, o1428–o1428.
- (54) Smith, G. D.; Bharadwaj, R. K. Quantum Chemistry Based Force Field for Simulations of HMX. *J. Phys. Chem. B* **1999**, *103*, 3570–3575.
- (55) Müller-Plathe, F. A simple nonequilibrium molecular dynamics method for calculating the thermal conductivity. *J. Chem. Phys.* **1998**, *106*, 6082.
- (56) Heino, P. Lattice-Boltzmann finite-difference model with optical phonons for nanoscale thermal conduction. *Comput. Math. Appl.* **2010**, *59*, 2351–2359.
- (57) Izvekov, S.; Chung, P. W.; Rice, B. M. Non-equilibrium molecular dynamics simulation study of heat transport in hexahydro-1,3,5-trinitro-s-triazine (RDX). *Int. J. Heat Mass Transfer* **2011**, *54*, 5623–5632.
- (58) Hague, J. P. Determining the phonon density of states from specific heat measurements via maximum entropy methods. *J. Phys. Condens. Matter* **2005**, *17*, 2397–2405.
- (59) Berens, P. H.; Mackay, D. H. J.; White, G. M.; Wilson, K. R. Thermodynamics and quantum corrections from molecular dynamics for liquid water. *J. Chem. Phys.* **1983**, *79*, 2375–2389.
- (60) Behler, J.; Parrinello, M. Generalized Neural-Network Representation of High-Dimensional Potential-Energy Surfaces. *Phys. Rev. Lett.* **2007**, *98*, 146401.
- (61) Bartók, A. P.; Payne, M. C.; Kondor, R.; Csányi, G. Gaussian Approximation Potentials: The Accuracy of Quantum Mechanics, without the Electrons. *Phys. Rev. Lett.* **2010**, *104*, 136403.
- (62) Thompson, A. P.; Swiler, L. P.; Trott, C. R.; Foiles, S. M.; Tucker, G. J. Spectral neighbor analysis method for automated generation of quantum-accurate interatomic potentials. *J. Comput. Phys.* **2015**, *285*, 316–330.
- (63) Cohen, N.; Benson, S. W. Estimation of heats of formation of organic compounds by additivity methods. *Chem. Rev.* **1993**, *93*, 2419–2438.
- (64) Constantinou, L.; Gani, R. New group contribution method for estimating properties of pure compounds. *AIChE J.* **1994**, *40*, 1697–1710.
- (65) Halko, N.; Martinsson, P.-G.; Tropp, J. A. Finding Structure with Randomness: Probabilistic Algorithms for Constructing Approximate Matrix Decompositions. *SIAM Rev.* **2011**, *53*, 217–288.
- (66) Martinsson, P.-G.; Rokhlin, V.; Tygert, M. A randomized algorithm for the decomposition of matrices. *Appl. Comput. Harmon. Anal.* **2011**, *30*, 47–68.
- (67) Cichocki, A.; Phan, A.-H. Fast Local Algorithms for Large Scale Nonnegative Matrix and Tensor Factorizations. *IEICE Trans. Fundam. Electron. Commun. Comput. Sci.* **2009**, *E92-A*, 708–721.
- (68) Févotte, C.; Idier, J. Algorithms for Nonnegative Matrix Factorization with the β -Divergence. *Neural Comput.* **2011**, *23*, 2421–2456.
- (69) Lee, D. D.; Seung, H. S. Learning the parts of objects by non-negative matrix factorization. *Nature* **1999**, *401*, 788–791.
- (70) Guillamet, D.; Schiele, B.; Vitria, J. Analyzing non-negative matrix factorization for image classification. *Object recognition supported by user interaction for service robots 2* 116–119, 2002.
- (71) Zhao, L.; Zhuang, G.; Xu, X. Facial expression recognition based on PCA and NMF. In *2008 7th World Congress on Intelligent Control and Automation* 6826–6829, 2008.
- (72) Sakano, M. N.; Strachan, A. Unsupervised learning using dimensionality reduction via matrix decomposition. <https://nanohub.org/resources/dimredmatdecmp>, 2020.
- (73) Rom, N.; et al. Density-Dependent Liquid Nitromethane Decomposition: Molecular Dynamics Simulations Based on ReaxFF. *J. Phys. Chem. A* **2011**, *115*, 10181–10202.
- (74) Chakraborty, D.; Muller, R. P.; Dasgupta, S.; Goddard, W. A. A detailed model for the decomposition of nitramines: RDX and HMX. *J. Comput.-Aided Mater. Des.* **2001**, *8*, 203–212.
- (75) Permann, C. J. et al. MOOSE: Enabling Massively Parallel Multiphysics Simulation. 2019.
- (76) MOOSEwebsite, Multiphysics object oriented simulation environment (moose) framework. 2020.
- (77) Knoll, D. A.; Keyes, D. E. Jacobian-free Newton–Krylov methods: a survey of approaches and applications. *J. Comput. Phys.* **2004**, *193*, 357–397.
- (78) Liu, L.; Liu, Y.; Zybin, S. V.; Sun, H.; Goddard, W. A. ReaxFF-lg: Correction of the ReaxFF Reactive Force Field for London Dispersion, with Applications to the Equations of State for Energetic Materials. *J. Phys. Chem. A* **2011**, *115*, 11016–11022.
- (79) Alzate-Vargas, L.; et al. Uncertainties in the predictions of thermo-physical properties of thermoplastic polymers via molecular dynamics. *Modell. Simul. Mater. Sci. Eng.* **2018**, *26*, No. 065007.
- (80) Philip, J. R. Transient Heat Conduction Between a Sphere and a Surrounding Medium of Different Thermal Properties. *Aust. J. Phys.* **1964**, *17*, 420–430.